

Swift Observations of the bright uncatalogued X-ray transient MAXI J1535-571

Lian Tao,^{1*} YuPeng Chen,¹ Can GÜNGÖR,¹ Yue Huang,¹ FangJun Lu,¹
JinLu Qu,¹ LiMing Song,¹ Liang Zhang,¹ Shu Zhang¹ and ShuangNan Zhang^{1,2,3}

¹Key Laboratory of Particle Astrophysics, Institute of High Energy Physics, Chinese Academy of Sciences, Beijing 100049, China

²National Astronomical Observatories, Chinese Academy of Sciences, Beijing 100012, China

³University of the Chinese Academy of Sciences, Beijing, China

Accepted 2018 August 03. Received 2018 July 07; in original form 2017 November 13

ABSTRACT

The black hole candidate MAXI J1535-571 is a recently discovered X-ray transient. We report on the monitoring observations of *Swift* Gamma-Ray Burst Mission during outburst. The source transits from the hard state to the intermediate state, and reaches the soft state; near the end of the outburst, it returns to the hard state passing through the low intermediate state, following a typical Q-shaped loop in the hardness-intensity diagram. During the high intermediate state, detailed spectral analyses using a multi-temperature disk model reveal that the disk luminosity is flatter than the inner disk temperature to the fourth power, and the disk temperature profile varies as the disk radius raised to the power of -0.5 , consistent with the behavior of a slim disk, implying that the disk structure has been modified due to the high luminosity of $\sim 10^{39}$ erg s $^{-1}$. Meanwhile, the column density increases with the Eddington ratio, suggesting that the outflow matters are driven by radiation pressure due to the high accretion rate.

Key words: stars: individual (MAXI J1535-571) — X-rays: binaries — accretion, accretion disks — black hole physics

1 INTRODUCTION

A Low-mass X-ray binary system with a black hole compact object usually accretes matter from a companion star via Roche-lobe overflow and demonstrates a transient behavior. Driven by instabilities in the accretion disk (Lasota 2001), it may undergo an outburst after a long quiescent period, accordingly, its luminosity can vary by many orders of magnitude. The spectra in the outburst are primarily contributed by two components, i.e., a standard thin accretion disk (Shakura & Sunyaev 1973) and a corona in a power-law form. In a typical outburst, the source usually undergo several different spectral states (e.g., Fender et al. 2004; Remillard & McClintock 2006; Done et al. 2007). At the initial onset phase of an outburst, it is in a hard state with the spectrum dominated by a hard power-law component, and a steady jet may be present in this period. As the accretion rate increases, the source goes through an intermediate state and then reaches a soft state. In the soft state, the accretion disk dominates the emission and the power law component becomes much softer, meanwhile, the

jet quenches. The source stays in soft state until the late fading stage of the outburst. Then it returns to an intermediate state with an intensity lower than the one in the previous intermediate state. At the end of an outburst, the source turns back to the hard state. Thus, through the outburst, a black hole transient typically follows an counterclockwise Q-shaped loop in the hardness-intensity diagram (HID) (e.g., Belloni et al. 2005; Belloni & Motta 2016).

In some giant outbursts, the luminosity can approach to or exceed the classical Eddington limit (e.g., Revnivtsev et al. 2002; Tomsick et al. 2005; Motta et al. 2017). The accretion disk can no longer keep its thin structure and becomes geometrically thick (slim disk, Abramowicz et al. 1988), in the meanwhile, advection becomes the dominant process. Photons are trapped in the disk and the emission is thus inefficient. The disk luminosity and inner disk temperature relationship is then expected to be flatter than that of the standard thin disk (Watarai et al. 2000).

In this study, we report on a giant outburst of a new X-ray transient, MAXI J1535-571, which exhibits clear spectral evolution during the outburst. The source was serendipitously discovered with the *Monitor of All-sky X-ray Image*

* E-mail: lian.taotao@gmail.com

(*MAXI*; Matsuo et al. 2009) Gas Slit Camera (GSC) and the *Neil Gehrels Swift Observatory* (*Swift*) Burst Alert Telescope (BAT; Barthelmy 2004) when it went into outburst on 2017 September 2nd (Negoro et al. 2017a; Markwardt et al. 2017). Using *Swift*/X-ray Telescope (XRT; Burrows et al. 2005) Photon Counting (PC) mode data with the exposure time of 3279 s, the corrected X-ray position of the source was reported to be R.A.=15^h35^m19.^s73, Decl.=−57°13′48.[″]1 (J2000.0) (Kennea et al. 2017). The X-ray flux in the 4.0–10.0 keV band was about 34 mCrab (Negoro et al. 2017a), and its *Swift*/XRT spectrum was well represented by an absorbed power-law model with a neutral hydrogen column density (N_{H}) of 3.6×10^{22} atoms cm^{-2} and a photon index of 1.53, indicating the source was in hard state (Kennea et al. 2017).

Follow-up X-ray observations of *MAXI* J1535-571 were performed. Its *MAXI*/GSC spectrum obtained on September 5 also agreed with an absorbed power-law model, but the photon index was about 1.84, softer than that obtained on September 2nd (Negoro et al. 2017b). N_{H} seemed to be stable (3.4×10^{22} cm^{-2}), but was larger than the line-of-sight Galactic column density, $N_{\text{H}} = 1.5 \times 10^{22}$ cm^{-2} (Kalberla et al. 2005), suggesting that the accretion disk or the dense interstellar gas might obscure the source.

The source continued to brighten and soften on September 10-11, and the *Swift*/BAT count rate in the 15–50 keV band started to decrease, indicating that the source might undergo a hard to soft state transition (Nakahira et al. 2017; Kennea 2017; Palmer et al. 2017). In the following *MAXI*/GSC observation taken on September 20, the source intensity in the 2–20 keV band increased to 5 Crab, and the photon index reached to the value of 2.9. The thermal component also appeared in the spectrum; the inner disk temperature was about 1.5 keV throughout the fitting with a multi-temperature disk blackbody model (`diskbb`¹) (Shidatsu et al. 2017). Later works performed by the *MAXI* team obtain a more detailed look at the state transition of the source (Nakahira et al. 2018). They argued that two counterclockwise circles appeared on the HID. The source stayed at the soft state until 2018 April 30; then it showed spectral hardening in *Swift*/XRT observations and went back to the hard state (Russell et al. 2018).

The *Swift*/XRT power density spectrum of September 11 showed a strong low-frequency quasi-periodic oscillation (QPO) with the first and second harmonics at 1.87 Hz and 3.87 Hz, respectively (Mereminskiy & Grebenev 2017). The QPOs also were detected by *Neutron star Interior Composition Explorer* (*NICER*; Gendreau et al. 2012) between September 12 and 13 (Gendreau et al. 2017). The frequency of the first harmonic drifted between 1.9 Hz and 2.8 Hz, with the fractional root-mean-squared (rms) amplitude to be 6%, while the frequency of the second harmonic drifted between 3.8 Hz and 5.6 Hz, with the fractional rms of 5% (Gendreau et al. 2017). Benefiting from the large effective area of *Insight*-HXMT, QPOs were also definitely detected in the energy band up to 100 keV (Huang et al. 2018). Recently, some works reported the detailed evolution of the QPO parameters (Mereminskiy et al. 2018; Shang et al. 2018).

Nuclear Spectroscopic Telescope Array (*NuSTAR*; Harrison et al. 2013) detected a broad Fe K_{α} line and a Compton hump with the peak energy of 30 keV on September 7 (Xu et al. 2018). Using a model combining a multi-temperature thermal component, a lamppost reflection model (`relxilllpCp`; Dauser et al. 2014; García et al. 2014) and an unblurred reflection model (`xillverCp`; García & Kallman 2010), they found the BH spin as $a > 0.84$, the inner disk radius as $r_{\text{in}} < 2.01 r_{\text{ISCO}}^2$, and the inclination angle of the inner disk $i(^{\circ}) = 57_{-2}^{+1}$. They also reported the existence of a broad iron emission line in the *NICER* spectra taken on September 13. Using the model of `relxill` (Dauser et al. 2014; García et al. 2014) which is a combination of a multi-temperature thermal component and a relativistic reflection, Gendreau et al. (2017) obtained a consistent BH spin, $a = 0.88_{-0.2}^{+0.1}$, but much lower inclination, $i(^{\circ}) = 27_{-5}^{+1}$. Miller et al. (2018) recently reanalyzed the *NICER* data and obtained a near-maximal spin of 0.994. Moreover, they found that the accretion disk is likely to be warped and the inclination of the inner disk is $i(^{\circ}) = 67 \pm 8$.

Multiwavelength observations of this source were also performed. The optical counterpart was identified by the 0.61m B&C Telescope at Mt. John Observatory. The magnitude in the SDSS *i*-band was 21^m.79, while no source was detected in the SDSS *g* and *r* bands, suggesting that the source might be a low mass X-ray binary (LMXB) (Scaringi & ASTR211 Students 2017). The near-infrared (NIR) counterpart was identified in the following observations taken on September 5, by the Small and Moderate Aperture Research Telescope System (SMARTS) 1.3m telescope at Cerro Tololo Inter-American Observatory (CTIO) (Dincer 2017). *Gemini* observed the source on October 2, and found that the source had faded by about 2^m.2 in the *H*-band. A Brackett- γ emission line appeared in the K-band spectrum with the line centroid at 21667 Å with the FWHM of 79.0 Å ($\sim 1090 \pm 60$ km/s) (Britt et al. 2017).

The radio counterpart of *MAXI* J1535-571 was discovered by the Australia Telescope Compact Array (ATCA) on September 5 (Russell et al. 2017). The flux densities at 5.5 GHz and 9.0 GHz had a power-law form with an index of 0.09 ± 0.03 , consistent with emission from a compact jet. The Atacama Large Millimetre/Sub-Millimetre Array (ALMA) and the ATCA then observed the radio source on September 11 and 12, respectively (Tetarenko et al. 2017). A spectral break between the 140–230 GHz was found, which means that the optically thick jet changed to optically thin at this frequency range.

Inferred from the X-ray and multiwavelength observations, *MAXI* J1535-571 differs from a neutron star. Its radio luminosity at 5 GHz is well above the limit of all known neutron star binaries, but consistent with the values of BH binaries (Russell et al. 2017). Moreover, its *MAXI*/GSC light curve shows rapid X-ray variability with no obvious pulsation (Negoro et al. 2017b) and is lack of X-ray bursts. Moreover, its unabsorbed flux of the 1–60 keV in the onset of the outburst is $\sim 3.1 \times 10^{-8}$ erg cm^{-2} s^{-1} ; assuming a typical distance of Galactic black holes (BHs) of 8 kpc, the luminosity is $\sim 2.4 \times 10^{38}$ erg s^{-1} and violates the classical Eddington limit of a neutron star (Negoro et al. 2017b). However,

¹ <https://heasarc.gsfc.nasa.gov/xanadu/xspec/manual/node159.html> ² r_{ISCO} is the innermost stable circular orbit.

the dynamical mass constraint is not available yet, thus we prefer to mention that it is still a BH candidate, instead of firmly conclude its BH nature.

In this paper, we particularly use *Swift* monitoring observations (Section 2) to investigate the spectral evolution and properties of the recently discovered BH candidate, MAXI J1535-571 (Section 3), and then discuss the results in Section 4.

2 OBSERVATIONS AND DATA REDUCTION

Monitoring of MAXI J1535-571 with *Swift* commenced on 2017 September 2. In order to study the outburst properties of the source, we search for all of *Swift*/XRT observations until 2018 May 14th. Due to its extreme brightness, except for the late fading stage, we only use the data taken in windowed timing (WT) mode. In the late fading stage, the data taken in photon counting (PC) mode are used instead as the source is very weak. The properties of the observations are listed in Table 2.

The *Swift*/XRT data are reduced using XSELECT, HEASoft v6.22, with XRT CALDB version 20170501. However, most of the observations are faced with several pileups due to the high count rates (> 100 cts s^{-1} , Table 1) of the source. We thus extract the counts by excluding the core using an annulus if pileup is present in the observation. The inner radius of the excluded region is selected so that the extracted count rate falls below 100 cts s^{-1} (method 1, Table 1). For comparison, we also investigate the level of pileup by increasing the excluded region and seeking for the key radius where the spectra is no longer soften (method 2, see Section 3.2 for more details) or the fraction of grade 0 events stay close to constant (method 3)³. Method 1 and 2 give a consistent result. Method 3, however, shows a trend towards a smaller excluded region, and thus is not strict as the method 1 and 2.

The outer radius of the extracted region is 20 pixels. For WT mode data, the background extraction region is an annulus centered at the source with the inner and the outer radii of 90 and 110 pixels, respectively. For PC mode data, the background extraction region is a source-free annulus centered at the source with the inner and the outer radii of 60 and 110 pixels, respectively. Using the `ftool xrtrmkarf` including the point-like PSF correction, ancillary response files are created and the ratios between the total fluence of the source and the fluence within the annular extraction region are estimated. The loss of counts due to pileup and bad pixels are then corrected using the fluence ratio. Finally, except for the last six observations (ObsID 10264048 – 10264053), the extracted spectra are rebinned to contain minimum 20 counts per bin using `grppha` in order to use χ^2 statistics in the spectral fits below (section 3.2). For ObsID 10264048 – 10264053, there are very few photons, the spectra are thus grouped with a minimum of 1 count in each bin, and we use C statistic in the spectral fits.

3 RESULTS

3.1 Light Curve and Hardness Ratio

As shown in the light curves (Figure 1) of *Swift*/BAT (15–50 keV band)⁴ and XRT (0.5–10 keV), the source went through a clear evolution and was extremely variable over the duration of the outburst. The hardness ratio, defined as the ratio of the count rates in the 4.0–10 keV to 0.5–4.0 keV bands, exhibited four distinguishable groups (Figure 1): it stayed around 0.5–0.6 at the beginning of the outburst (group A), but suddenly decreased to ~ 0.4 on MJD 58007 (group B), and then stayed close to that level; after a ninety-day interval that *Swift* did not observe the source, the hardness ratio was less than 0.2, which is much smaller than the previous values (group C); near the end of the outburst, the hardness ratio suddenly jumped up to a high level, with a value of around 0.6, similar to that of the beginning of the outburst (group D). Different groups in the hardness ratio may indicate different spectral state. Therefore, the source may undergo several state transitions over the course of the outburst.

HIDs are powerful tools to distinguish different spectral states. We thus plotted two HIDs using *Swift*/XRT observations in the energy range of 0.5–10.0 keV from MJD 57999 to MJD 58252 and the simultaneous *MAXI*/GSC data⁵ in the energy range of 2–20 keV, and marked the four groups above with the same symbols used for the hardness ratio curve (Figure 2). Near the end of the outburst, the source was too weak to be detected by *MAXI*, thus group D is not in the *MAXI* HID. Two HIDs follow a similar X-ray spectral evolution track, similar to the typical Q-shaped loop of BH binaries (Figure 4 of Belloni & Motta 2016). Group A and D are in the right branches of the HIDs, which means that the source was in the hard state of raising stage and fading stage, respectively. Group C is in the left branches of the HIDs, which indicates that the source was in the soft state. Group B goes through a small counter clockwise loop, and it is referred to the intermediate state. Since several pileups are present in most of *Swift*/XRT observations, the central source pixels are excluded and the final enough count rate were not enough to do detailed timing analyses. However, benefiting from pileup-free and large effective area of *Insight*-HXMT, based on the timing analyses, Huang et al. (2018) argued that the source was in the intermediate state from MJD 58008 to MJD 58019, which is consistent with our results. Moreover, the spectral analyses explained in Section 3.2 verifies our state identification.

3.2 Spectral Properties

The XSPEC v12.9.1m software package (Arnaud 1996) is used to perform the spectral fits. For the absorption calculation, the absorption model (`tbabs`) with Wilms et al. (2000) abundances and Verner et al. (1996) cross-sections, is implemented. The *Swift*/XRT data below 1.0 keV are ignored during the spectral fits in order to exclude the low-energy spectral residuals in windowed timing mode. For PC

³ <http://www.swift.ac.uk/analysis/xrt/pileup.php>

⁴ <https://swift.gsfc.nasa.gov/results/transients/weak/MAXIJ1535-571/>

⁵ http://134.160.243.77/star_data/J1535-572/J1535-572.html

Table 1. General properties of *Swift*/XRT Observations sampled in this paper. Most of the *Swift*/XRT data are taken in windowed timing mode except some observations in the late fading stage. For these observations in the late stage, we use the data obtained in photon counting mode instead. Hard – hard state; HIM – hard intermediate state; SIM – soft intermediate state; Soft – soft state.

ObsID	Observed date (day)	Observed date (MJD)	Exposure (s)	Count rate ^b (cts s ⁻¹)	Count rate ^c (cts s ⁻¹)	Pixels ^d	State
770431000	2017-09-02 20:07:41	57998.84	1615.86	9.79 ± 0.08	9.31 ± 0.08	0	Hard
770502000	2017-09-03 09:02:43	57999.38	75.03	20.8 ± 0.5	19.9 ± 0.6	0	Hard
770656000	2017-09-04 14:05:48	58000.59	15.60	74 ± 2	77 ± 2	0	Hard
770656001	2017-09-04 17:12:35	58000.72	988.80	71.1 ± 0.3	76.1 ± 0.3	0	Hard
10264002	2017-09-06 00:41:58	58002.03	449.23	139.1 ± 0.6	142.0 ± 0.8	2	Hard
10264003	2017-09-08 06:40:51	58004.28	4948.53	221.7 ± 0.2	306.1 ± 0.5	3	Hard
771371000	2017-09-08 11:39:18	58004.49	69.12	236 ± 2	335 ± 4	4	Hard
10264004	2017-09-11 06:34:43	58007.27	1089.61	510.4 ± 0.7	618 ± 2	7	HIM
10264005	2017-09-12 06:19:10	58008.26	899.61	543.7 ± 0.8	948 ± 4	9	HIM
10264007	2017-09-13 00:11:05	58009.01	889.45	661.2 ± 0.9	983 ± 4	9	HIM
10264006	2017-09-14 22:19:59	58010.93	1074.61	640.5 ± 0.8	975 ± 3	9	HIM
10264008	2017-09-15 09:19:30	58011.39	984.64	643.2 ± 0.8	951 ± 3	8	HIM
10264009	2017-09-16 02:47:14	58012.12	1059.79	644.5 ± 0.8	964 ± 3	9	HIM
88245001	2017-09-17 04:17:53	58013.18	2223.08	690.1 ± 0.6	1613 ± 4	11	HIM
10264010	2017-09-18 04:13:31	58014.18	1104.61	783.5 ± 0.8	1352 ± 5	10	HIM
10264011	2017-09-19 08:56:26	58015.37	989.39	29.5 ± 0.2	2041 ± 13	0 ^e	SIM
88245002	2017-09-20 23:13:58	58016.97	954.61	933.6 ± 1.0	1728 ± 6	11	SIM
88245003	2017-09-21 00:48:59	58017.03	1014.19	1012.0 ± 1.0	1984 ± 8	13	SIM
10264012	2017-09-22 15:17:53	58018.64	1189.21	998.4 ± 0.9	2139 ± 7	13	SIM
10264013	2017-09-23 02:23:05	58019.10	1009.60	1066.7 ± 1.0	2228 ± 8	13	SIM
10264014	2017-09-24 02:29:57	58020.10	599.21	836.4 ± 1.2	2070 ± 10	13	SIM
10264015	2017-09-25 21:30:52	58021.90	899.49	972.9 ± 1.0	1984 ± 8	13	SIM
10264016	2017-09-26 18:15:01	58022.76	909.22	942.4 ± 1.0	1923 ± 8	13	SIM
10264017	2017-09-27 16:40:13	58023.70	859.22	875.5 ± 1.0	2079 ± 8	11	SIM
10264018	2017-09-28 18:04:31	58024.75	1044.61	880.3 ± 0.9	1858 ± 7	12	SIM
10264019	2017-09-29 18:00:51	58025.75	964.65	778.8 ± 0.9	1938 ± 7	12	SIM
10264020	2017-09-30 18:01:05	58026.75	889.62	899.3 ± 1.0	2401 ± 10	13	SIM
10264021	2017-10-01 17:51:20	58027.74	874.62	742.2 ± 0.9	1480 ± 6	12	SIM
10264022	2017-10-02 17:48:25	58028.74	1109.61	842.3 ± 0.9	1590 ± 6	12	SIM
10264023	2017-10-03 17:46:07	58029.74	1004.61	878.5 ± 0.9	1507 ± 6	11	SIM
10264024	2017-10-04 17:44:51	58030.74	964.61	358.1 ± 0.6	1307 ± 5	11	SIM
10264025	2017-10-05 15:55:38	58031.66	604.61	754.5 ± 1.1	1294 ± 6	10	SIM
10264026	2017-10-06 11:08:37	58032.47	1154.61	867.0 ± 0.9	1519 ± 5	11	SIM
10264027	2017-10-07 04:37:47	58033.19	1024.61	429.3 ± 0.6	1510 ± 5	11	SIM
10264028	2017-10-08 05:57:40	58034.25	974.61	814.6 ± 0.9	1655 ± 7	12	SIM
10264029	2017-10-09 10:54:12	58035.46	1059.61	560.1 ± 0.7	1048 ± 4	10	SIM
10264030	2017-10-10 12:07:37	58036.51	994.06	705.6 ± 0.8	1263 ± 5	10	SIM
10264031	2017-10-11 07:35:39	58037.32	854.62	651.2 ± 0.9	976 ± 4	9	SIM
88245004	2017-10-22 23:42:52	58048.99	2088.03	434.1 ± 0.5	602 ± 2	6	SIM
88246001	2017-10-24 23:31:53	58050.98	1528.20	392.9 ± 0.5	560 ± 2	6	SIM
10491002	2018-01-19 08:08:13	58137.34	1119.61	171.7 ± 0.4	195.2 ± 0.7	3	Soft
10264032	2018-03-17 19:13:28	58194.80	279.62	34.1 ± 0.3	55.7 ± 0.6	0	Soft
10264033	2018-03-18 10:47:57	58195.45	1370.35	48.1 ± 0.19	50.1 ± 0.2	0	Soft
10264034	2018-03-24 21:16:57	58201.89	1859.22	28.93 ± 0.12	37.78 ± 0.18	0	Soft
10264035	2018-03-26 13:28:47	58203.56	1409.22	19.56 ± 0.12	30.4 ± 0.2	0	Soft
10264036	2018-03-28 13:23:57	58205.56	2015.28	25.39 ± 0.11	27.96 ± 0.13	0	Soft
10264037	2018-03-30 02:03:57	58207.09	1910.28	23.88 ± 0.11	26.68 ± 0.14	0	Soft
10264038	2018-04-01 20:30:56	58209.86	509.46	20.2 ± 0.2	19.8 ± 0.2	0	Soft
10264039	2018-04-07 18:47:57	58215.79	2244.15	8.09 ± 0.06	9.21 ± 0.08	0	Soft
10264040	2018-04-09 11:41:57	58217.49	2131.63	7.36 ± 0.06	7.00 ± 0.07	0	Soft
10264041	2018-04-12 00:32:57	58220.03	1949.17	4.23 ± 0.05	4.32 ± 0.06	0	Soft
10264042	2018-04-13 14:35:57	58221.61	1719.23	3.08 ± 0.04	3.13 ± 0.06	0	Soft
10264043	2018-04-16 23:58:57	58225.00	1115.41	2.14 ± 0.04	1.53 ± 0.05	0	Soft
10264044	2018-04-18 15:51:57	58226.66	249.45	1.47 ± 0.08	1.21 ± 0.09	0	Soft
10264045	2018-04-21 22:21:57	58229.94	1063.92	0.82 ± 0.03	0.53 ± 0.04	0	Soft
10264046 ^a	2018-04-24 22:04:57	58232.92	1703.15	0.180 ± 0.010	0.195 ± 0.011	0	IM
10264047 ^a	2018-04-26 02:32:56	58234.11	1797.36	0.118 ± 0.008	0.129 ± 0.009	0	IM

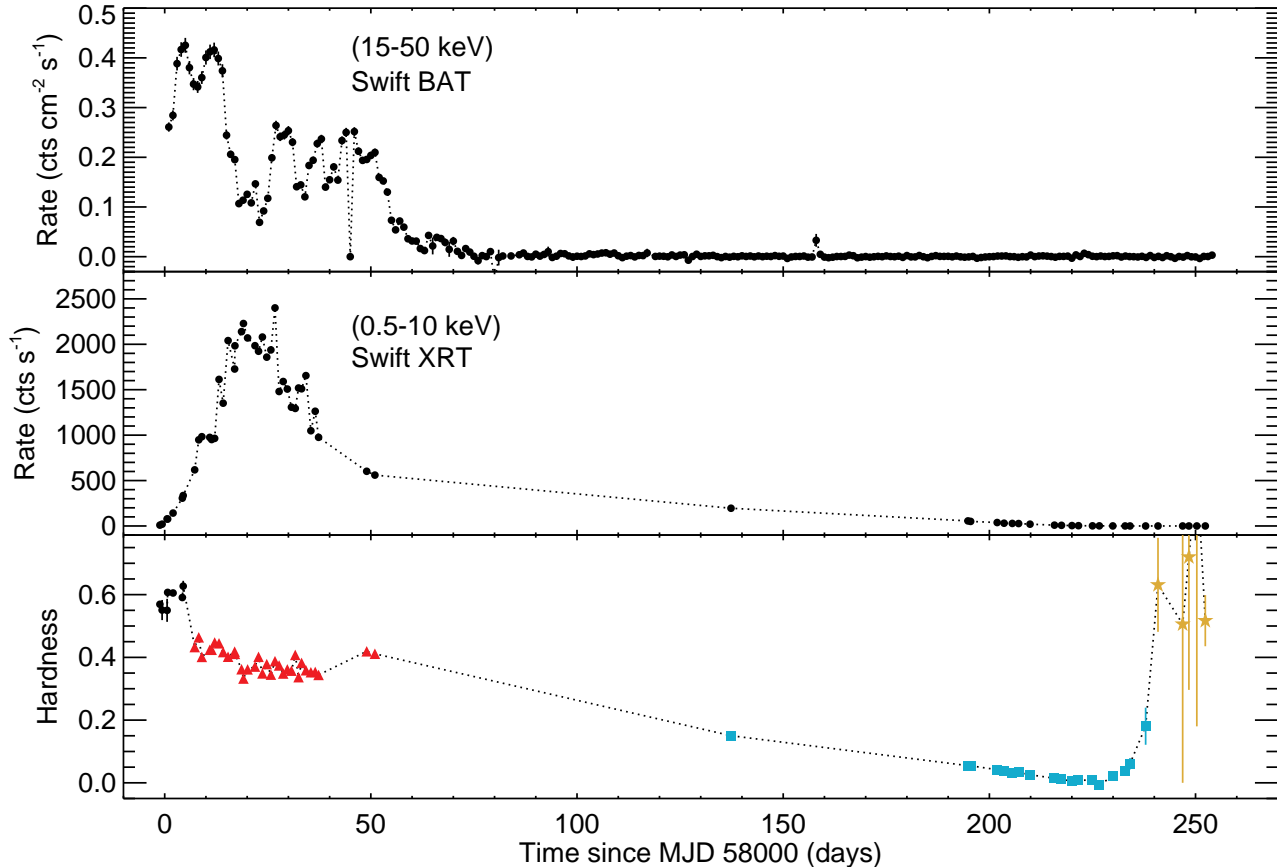


Figure 1. The 15–50 keV *Swift*/BAT count rate (top panel), the 0.5–10 keV *Swift*/XRT count rate (middle panel), and the hardness ratio of the *Swift*/XRT hard band (4.0–10 keV) to the soft band (0.5–4.0 keV; the bottom panel). Black dots, red triangles, blue squares and golden stars in the bottom panel indicate four distinguishable groups in the hardness ratio, respectively.

Table 1 – *continued*

ObsID	Observed date (day)	Observed date (MJD)	Exposure (s)	Count rate ^b (cts s ⁻¹)	Count rate ^c (cts s ⁻¹)	Pixels ^d	State
10264048 ^a	2018-04-29 21:21:57	58237.89	1771.22	0.042 ± 0.005	0.049 ± 0.006	0	Hard
10264049 ^a	2018-05-02 21:23:57	58240.90	1854.74	0.041 ± 0.005	0.047 ± 0.005	0	Hard
10264050 ^a	2018-05-08 20:48:58	58246.87	1790.09	0.005 ± 0.003	0.005 ± 0.003	0	Hard
10264051 ^a	2018-05-10 09:17:57	58248.39	1903.64	0.006 ± 0.002	0.009 ± 0.003	0	Hard
10264052 ^a	2018-05-12 07:17:56	58250.31	1003.63	0.006 ± 0.002	0.008 ± 0.003	0	Hard
10264053 ^a	2018-05-14 08:41:38	58252.37	1470.92	0.125 ± 0.009	0.143 ± 0.011	0	Hard

^aThe observations are taken in photon counting mode.

^bThe observed count rates, which are not corrected for bad pixels, background and pileup.

^cThe count rates in the 0.5–10.0 keV band have been corrected for bad pixels, background and pileup, using the PSF correction factor in `xrtmkarf`.

^dThe radii of the excluded region.

^eDuring this observation, *Swift* partly missed the source.

mode, the spectra in the energy range of 0.3–10.0 keV is adopted to the spectral fits. If pileup is present in an observation, the level of pileup is investigated by increasing the excluded region. We find that the photon index (Γ) stays stable when using the radius listed in Table 1, and the typical change in Γ is less than 0.02 when continuing to increase the excluded region. The spectra of BH binaries are usually a composite of a thermal component, represented by a `diskbb` model, and a nonthermal component, represented by

a power-law model (Remillard & McClintock 2006). We thus experiment several models, i.e., a single power-law, a single `diskbb` and a two-component model consisting of power-law and disk components, to explore the significance of the disk and power-law components. The two-component model is preferred only if the F-test probability is low (< 0.05). However, near the end of the outburst (ObsID 10264046 – 10264053), the source is so weak, therefore count rates are not enough to decide the best fitting model, we thus inferred

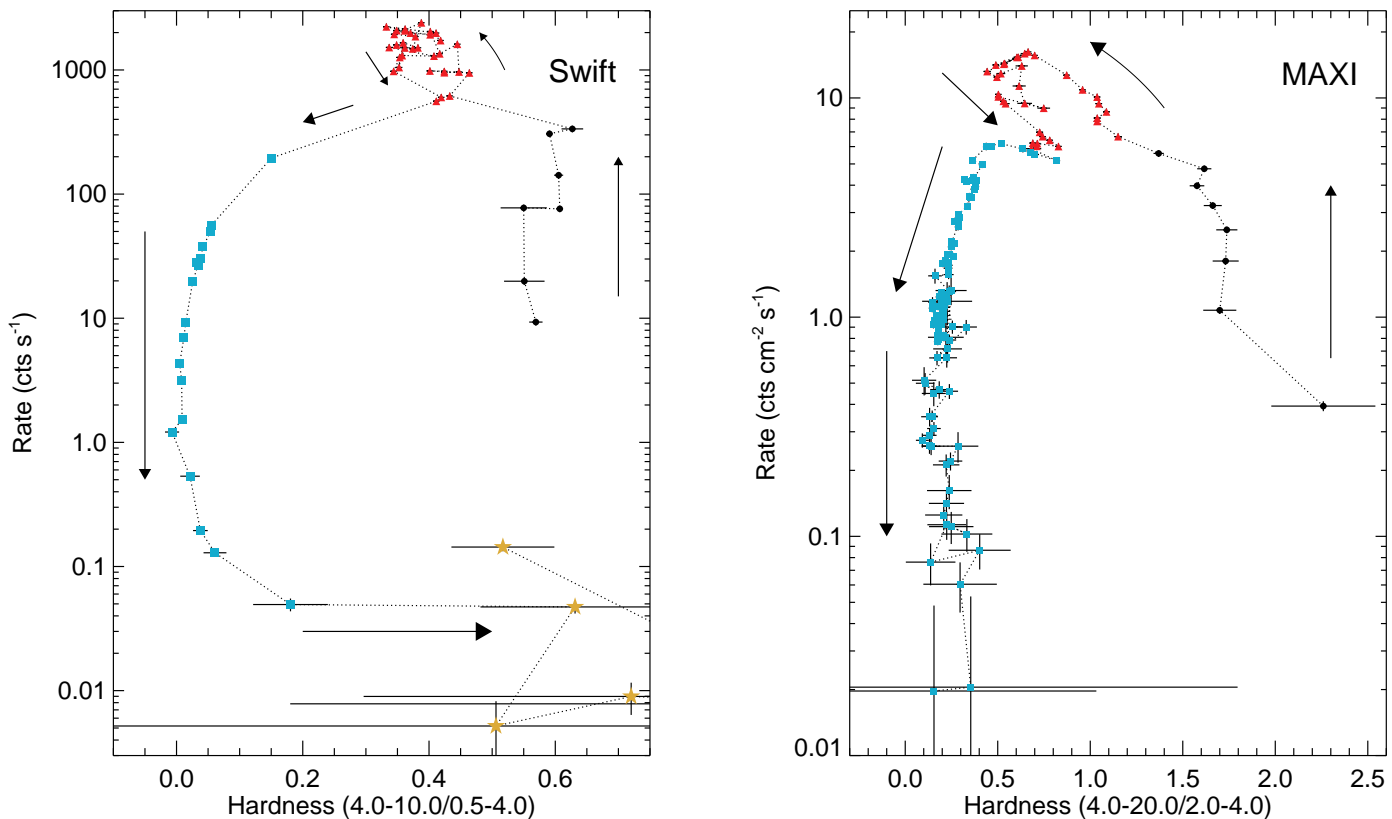


Figure 2. *Swift*/XRT and *MAXI*/GSC hardness-intensity diagrams of the source. Left panel: *Swift*/XRT HID. Intensities here are the count rates in the 0.5–10.0 keV, while hardness values are obtained using the ratio of 4–10 keV to 0.5–4.0 keV count rates. Right panel: *MAXI*/GSC HID. Intensities are the count rates in the 2–20 keV, while hardness values are the ratios of 4–20 keV to 2.0–4.0 keV count rates. The symbols here are the same as Figure 1. Arrows show the evolutionary track of the outburst.

it from the hardness ratio (Figure 1). For ObsID 10264046 – 10264047, the hardness ratio started to increase and the source passed through the hard state after four days, thus the two-component model is used. For ObsID 10264048 – 10264053, a single power-law is preferred as the source has already come back to the hard state. The models adopted are summarized in Table 1.

The X-ray absorption column density N_{H} , the photon index Γ , the inner disk temperature T_{in} , the square root of the normalization of the diskbb model ($N_{\text{disk}} = R_{\text{in}}(\text{km}) * D_{10}^{-1} * \sqrt{\cos(i)}$) are shown in Figure 3. The absorbed flux of the power-law and disk components in the 0.5–10.0 keV band, and the evolution of the ratios of the disk component flux to the total flux are shown in Figure 4. Parameter errors around the peak of outburst are larger than that in the raising stage and early fading stage, which seems to be in strong contrast with the expected uncertainty in statistics. However, we should note that the ‘detected’ counts are similar in these stages due to the pileup-excluding criteria ($< 100 \text{ cts s}^{-1}$), and the PSF correction factor in *xrtmkarf* are needed to correct the ‘real’ counts. Therefore, although the ‘detected’ statistical errors in these stages are similar, the actual uncertainties around the outburst peak became much larger due to a large PSF correction factor.

Compared with the Galactic absorption column density ($N_{\text{H}} = 1.5 \times 10^{22} \text{ cm}^{-2}$, Kalberla et al. 2005), N_{H} show an

obvious excess in the whole outburst, indicating that some intrinsic materials, such as the accretion disk, interstellar gas and outflow matter, may obscure the source. Moreover, N_{H} evolves along the outburst and reaches its peak value around the outburst maxima.

At the beginning of the outburst (MJD 57999 – 58004), the spectra were hard ($\Gamma \sim 1.5$), and the disk component was cool ($T_{\text{in}} < 0.5 \text{ keV}$) and weak (disk fraction $f_{\text{disk}} < 5\%$), consistent with the expectations of the hard state. As the accretion rate increasing, the source entered into the intermediate state. The power-law component became softer and the disk component started to be significant in the flux. Upon closer inspection, there were three parts in this state (Figure 3 and 4): MJD 58007 – 58014 (ObsID 10264004 – 10264010, part 1), MJD 58015 – 58037 (ObsID 10264011 – 10264031, part 2) and MJD 58049 – 58051 (ObsID 88245004 – 88246001, part3). Γ were about 2.5 in part 2, larger than that of parts 1 and 3 ($\Gamma \sim 2.0$); the inner disk temperature of part 2 had a significantly higher level, while the inner disk radius (N_{disk}) were much lower than that of parts 1 and 3; f_{disk} of part 2 were larger, so the disk component was stronger. Although we could not perform the timing analysis with *Swift*/XRT observations due to pileup effect, the timing results of *Insight*-HXMT found that the fractional rms over 0.1–32 Hz (1–12 keV) decreased from $\sim 15\%$ on MJD 58014 to 1.9% on MJD 58015 and meanwhile QPOs switched from type C to type B (Huang et al. 2018). Inferred

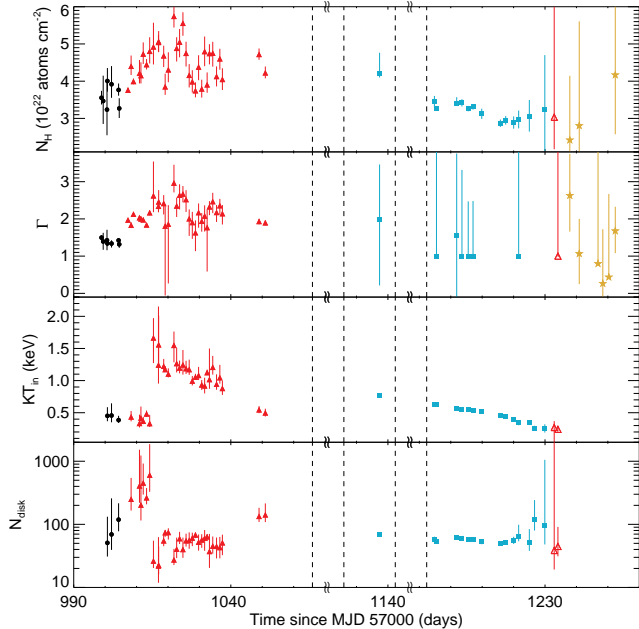


Figure 3. Evolution of *Swift*/XRT spectral parameters. The fixed parameters or the one with unconstrainable errors are not plotted in this figure. N_{H} is the X-ray absorption column density; Γ is the photon index; T_{in} is the inner disk temperature; $N_{\text{disk}} = R_{\text{in}}(\text{km}) * D_{10}^{-1} * \sqrt{\cos(i)}$ is the square root of the normalization of the diskbb model, where $R_{\text{in}}(\text{km})$ is the inner disk radius, D_{10} is the source distance in units of 10 kpc, and i is the angle of the disk. We marked different states using the same symbols as Figure 1, except for ObsID 10264046 – 10264047, which are revised as intermediate state based on spectral properties; hard state during the outburst rise (black dots), intermediate state during the outburst rise (red filled triangles), soft state (blue squares), intermediate state in the fading stage (red open triangles), hard state in the fading stage (golden stars).

from the spectral and timing properties, part 1 is in hard intermediate (HIM) state, while part 2 is soft intermediate (SIM) state. We also refer to part 3 as a hard intermediate state because the spectral properties are similar to that of part 1, even though there are no timing studies during this period. After a ninety-day interval, when *Swift* observed the source again (MJD 58137), we found that the disk component dominated the emission with $f_{\text{disk}} > 80\%$ and N_{disk} was stable, indicating that the source may go through another soft intermediate state, which was not detected due to the lack of observations, and reached the soft state finally. The source stayed in the soft state until MJD 58230. Around MJD 58233–58234 (ObsID 10264046 – 10264047), f_{disk} decreased to be less than 40%, and four days later, the source was in the hard state again. We thus revise ObsID 10264046 and 10264047 as intermediate state. For convenience, the state classifications are listed in Table 2.

3.3 Disk Component

In general, the disk component of black hole can be well described with a standard thin disk (Shakura & Sunyaev 1973). Its disk luminosity L_{disk} and the inner disk temperature T_{in} follows $L_{\text{disk}} \propto T_{\text{in}}^4$, and its radial temperature

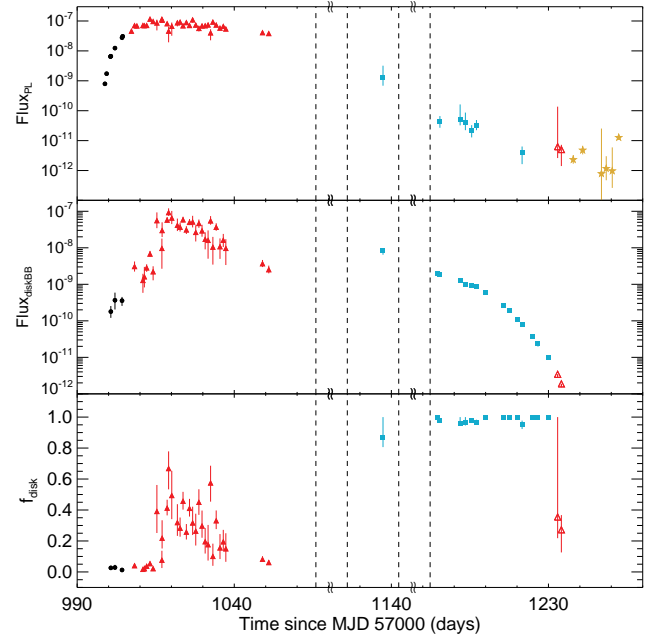


Figure 4. Evolution of absorbed flux of the power-law and diskbb models in the energy range of the 0.5–10 keV, and the flux ratio of the disk component. Flux here is in units of $\text{erg cm}^{-2} \text{ s}^{-1}$. Different states are marked using the same colored symbols as Figure 3.

profile varies as $T(R) \propto R^{-0.75}$. However, the disk structure may be modified if the source is bright. The peak flux of MAXI J1535-571 is ~ 5 Crab, we thus need to test whether its disk component follows the standard scenario. As some key parameters, i.e, the distance D and the inclination i , are not well constrained, we thus use the disk luminosity $L_{\text{disk}} * D_{10}^{-2}$ and the square root of the normalization of the diskbb model, $N_{\text{disk}} = R_{\text{in}}(\text{km}) * D_{10}^{-1} * \sqrt{\cos(i)}$ instead, to test the relations $L_{\text{disk}} \propto T_{\text{in}}^\alpha$ and $T(R) \propto R^{-p}$.

$L_{\text{disk}} * D_{10}^{-2}$ versus T_{in} , as shown in the left panel of Figure 5, follows a tight relation, except for the observations which the source was in the high intermediate state. We thus fit L_{disk} versus T_{in} in the high intermediate state (middle panel of Figure 5) and the remaining states (right panel of Figure 5) to a power-law function, respectively, and found that α is 1.06 ± 0.14 and 4.24 ± 0.11 . Moreover, we also test the $L_{\text{disk}} \propto T_{\text{in}}^\alpha$ relation if only fitting data in the SIM state and soft state, respectively, and obtain $\alpha = 1.0 \pm 0.4$ for the SIM state and $\alpha = 4.20 \pm 0.12$ for the soft state.

T versus R are plotted in Figure 6. In the high intermediate state (middle panel of Figure 6), N_{disk} and T_{in} appear to have a robust correlation. The radial temperature profile has a flatter p of 0.54 ± 0.03 if fitting to a power-law function ($T(R) \propto R^{-p}$). The data in the right panel of Figure 6 show clearly that the soft state has an approximately constant radius, consistent with the expectation that the inner disk extends to the innermost stable circular orbit (ISCO) in the soft state. N_{disk} in the hard state is not significantly larger than that in the soft state, indicating that the inner disk is not significantly truncated, consistent with the result of Xu et al. (2018), which report an inner disk radius of $< 2.01 R_{\text{ISCO}}$ in the hard state based on the reflection modeling of *NuSTAR* data.

Table 2. Spectral Fitting of MAXI J1535-571. PL: power-law model; PLBB: power-law + `diskbb`; BB: `diskbb`. N_{H} is the X-ray absorption column density in units of 10^{22} atoms cm^{-2} ; Γ is the power-law photon index; kT_{in} is the accretion disk temperature of the `diskbb` model in units of keV; N_{disk} is the square root of the normalization of the `diskbb` model, $N_{\text{disk}} = R_{\text{in}}(\text{km}) * D_{10}^{-1} * \sqrt{\cos(i)}$; All errors and limits are at 90% confidence level.

ObsID	Model	N_{H} (10^{22} cm^{-2})	Γ	kT_{in} (keV)	N_{disk}	χ^2/dof (C^2/dof) ^f
770431000	PL	3.6 ± 0.2	1.50 ± 0.07	410.9/450
770502000	PL	$3.5^{+0.7}_{-0.6}$	1.4 ± 0.2	49.1/58
770656000	PL	$3.2^{+0.8}_{-0.7}$	1.4 ± 0.3	45.0/42
770656001	PLBB	4.0 ± 0.3	$1.34^{+0.06}_{-0.07}$	$0.45^{+0.14}_{-0.08}$	50^{+80}_{-20}	736.0/700
10264002	PLBB	$3.9^{+0.5}_{-0.4}$	$1.34^{+0.09}_{-0.11}$	$0.46^{+0.19}_{-0.11}$	70^{+190}_{-30}	583.6/608
10264003	PLBB	3.8 ± 0.2	1.42 ± 0.02	$0.39^{+0.07}_{-0.04}$	120^{+100}_{-40}	984.4/855
771371000	PL	3.3 ± 0.3	1.32 ± 0.10	188.6/227
10264004	PL	3.76 ± 0.06	1.97 ± 0.03	763.0/696
10264005	PLBB	$4.4^{+0.3}_{-0.2}$	$1.83^{+0.07}_{-0.08}$	$0.44^{+0.09}_{-0.07}$	250^{+290}_{-90}	695.6/672
10264007	PL	3.99 ± 0.08	2.13 ± 0.03	701.5/661
10264006	PLBB	$4.2^{+0.4}_{-0.3}$	2.03 ± 0.06	$0.33^{+0.14}_{-0.06}$	410^{+1120}_{-190}	700.9/681
10264008	PLBB	$4.2^{+0.4}_{-0.2}$	$2.00^{+0.07}_{-0.08}$	$0.42^{+0.18}_{-0.12}$	200^{+1030}_{-90}	681.5/682
10264009	PLBB	4.7 ± 0.3	1.98 ± 0.06	$0.37^{+0.06}_{-0.05}$	450^{+470}_{-160}	781.1/689
88245001	PLBB	$4.45^{+0.15}_{-0.13}$	1.84 ± 0.05	$0.48^{+0.05}$	260^{+110}_{-60}	859.2/769
10264010	PLBB	$4.8^{+0.4}_{-0.3}$	$2.17^{+0.06}_{-0.07}$	$0.33^{+0.13}_{-0.05}$	600^{+1300}_{-300}	718.1/692
10264011	PLBB	$4.9^{+0.6}_{-0.5}$	$2.6^{+0.9}_{-0.4}$	$1.7^{+0.3}_{-0.4}$	26^{+29}_{-6}	486.1/516
88245002	PLBB	$5.0^{+0.2}_{-0.3}$	$2.34^{+0.15}_{-0.16}$	$1.2^{+0.9}_{-0.3}$	22^{+41}_{-19}	687.8/660
88245003	PLBB	5.1 ± 0.3	$2.5^{+0.3}_{-0.2}$	$1.6^{+0.3}_{-0.3}$	23^{+22}_{-6}	709.8/645
10264012	PLBB	4.7 ± 0.3	$2.4^{+0.2}_{-0.3}$	$1.22^{+0.11}_{-0.08}$	55^{+14}_{-10}	789.9/648
10264013	PLBB	$3.9^{+0.4}_{-0.2}$	$1.8^{+0.5}_{-1.9}$	$1.17^{+0.05}_{-0.04}$	74^{+7}_{-11}	623.4/615
10264014	PLBB	$4.3^{+0.5}_{-0.3}$	$1.9^{+0.5}_{-1.6}$	$1.10^{+0.09}_{-0.05}$	75^{+12}_{-17}	597.5/577
10264015	PLBB	$5.7^{+0.4}_{-0.3}$	$3.0^{+0.5}_{-0.3}$	$1.5^{+0.2}_{-0.3}$	27^{+13}_{-5}	678.8/618
10264016	PLBB	$4.9^{+0.4}_{-0.3}$	$2.3^{+0.3}_{-0.3}$	$1.27^{+0.24}_{-0.14}$	40^{+21}_{-11}	658.2/634
10264017	PLBB	$5.1^{+0.3}_{-0.4}$	$2.6^{+0.3}_{-0.4}$	$1.20^{+0.11}_{-0.08}$	60^{+17}_{-11}	650.8/611
10264018	PLBB	5.6 ± 0.3	2.7 ± 0.2	$1.25^{+0.23}_{-0.15}$	40^{+22}_{-11}	636.2/632
10264019	PLBB	$4.8^{+0.3}_{-0.4}$	$2.5^{+0.2}_{-0.3}$	$1.19^{+0.12}_{-0.08}$	55^{+16}_{-11}	637.5/622
10264020	PLBB	4.2 ± 0.3	$2.0^{+0.2}_{-0.5}$	$1.17^{+0.15}_{-0.08}$	56^{+19}_{-15}	658.5/634
10264021	PLBB	4.0 ± 0.3	$1.9^{+0.3}_{-0.4}$	$0.99^{+0.08}_{-0.07}$	61^{+13}_{-16}	644.7/632
10264022	PLBB	3.7 ± 0.2	$1.6^{+0.3}_{-0.5}$	$1.06^{+0.05}_{-0.04}$	68^{+6}_{-8}	699.5/651
10264023	PLBB	$4.4^{+0.3}_{-0.4}$	$2.2^{+0.2}_{-0.4}$	$1.08^{+0.13}_{-0.07}$	52^{+17}_{-14}	607.4/631
10264024	PLBB	3.8 ± 0.2	$1.9^{+0.2}_{-0.3}$	$0.93^{+0.08}$	57^{+13}_{-14}	678.7/645
10264025	PLBB	4.8 ± 0.4	$2.1^{+0.3}_{-0.4}$	$0.92^{+0.13}_{-0.12}$	60 ± 20	612.3/612
10264026	PLBB	$3.9^{+0.3}_{-0.2}$	$1.8^{+0.5}_{-1.2}$	$1.13^{+0.04}$	64^{+6}_{-9}	658.8/645
10264027	PLBB	$4.7^{+0.2}_{-0.3}$	2.3 ± 0.2	$1.02^{+0.48}_{-0.15}$	37^{+33}_{-17}	681.4/656
10264028	PLBB	$4.8^{+0.3}_{-0.4}$	$2.5^{+0.2}_{-0.3}$	$1.21^{+0.18}_{-0.11}$	45^{+19}_{-11}	599.2/618
10264029	PLBB	4.1 ± 0.3	$2.2^{+0.2}_{-0.3}$	$0.94^{+0.15}_{-0.09}$	45^{+17}_{-16}	689.1/654
10264030	PLBB	4.6 ± 0.3	2.4 ± 0.2	$1.05^{+0.20}_{-0.09}$	43^{+20}_{-14}	656.0/644
10264031	PLBB	4.0 ± 0.3	$2.1^{+0.2}_{-0.3}$	$0.88^{+0.12}_{-0.10}$	51^{+17}_{-19}	581.9/621
88245004	PLBB	$4.72^{+0.16}_{-0.15}$	$1.93^{+0.07}_{-0.08}$	$0.55^{+0.06}_{-0.05}$	130^{+40}_{-30}	885.3/760
88246001	PLBB	$4.23^{+0.17}_{-0.15}$	$1.90^{+0.06}_{-0.07}$	0.50 ± 0.06	140^{+60}_{-40}	694.2/729
10491002	PLBB	$4.21^{+0.15}_{-0.11}$	$2.0^{+1.5}_{-1.8}$	0.77 ± 0.02	69^{+3}_{-4}	508.7/510
10264032	BB	3.45 ± 0.15	...	0.623 ± 0.016	58^{+6}_{-5}	241.1/253
10264033	PLBB	3.27 ± 0.06	$1.0^{+4.6}_{-0.0} c$	$0.626^{+0.008}_{-0.007}$	53 ± 2	448.2/404
10264034	PLBB	$3.41^{+0.16}_{-0.08}$	$1.5^{+2.2}_{-2.5} c$	$0.563^{+0.011}_{-0.013}$	62^{+4}_{-3}	381.3/371
10264035	PLBB	3.42 ± 0.10	$1.0^{+2.3}_{-0.0} c$	$0.547^{+0.011}_{-0.012}$	61 ± 4	364.9/323
10264036	PLBB	$3.26^{+0.06}_{-0.07}$	$1.0^{+1.5}_{-0.0} c$	0.543 ± 0.007	58^{+3}_{-2}	391.5/353
10264037	PLBB	3.31 ± 0.07	$1.0^{+1.5}_{-0.0} c$	$0.539^{+0.008}_{-0.009}$	58 ± 3	442.4/347
10264038	BB	$3.12^{+0.14}_{-0.13}$...	0.522 ± 0.013	53^{+5}_{-4}	245.3/226
10264039	BB	2.87 ± 0.10	...	0.459 ± 0.009	50^{+4}_{-3}	275.5/247
10264040	BB	$2.95^{+0.12}_{-0.11}$...	0.435 ± 0.010	51^{+5}_{-4}	209.2/227
10264041	BB	$2.88^{+0.17}_{-0.16}$...	0.390 ± 0.012	55^{+8}_{-6}	184.0/171
10264042	PLBB	$2.96^{+0.25}_{-0.23}$	$1.0^{+5.6}_{-0.0} c$	$0.354^{+0.019}_{-0.05}$	65^{+33}_{-11}	136.6/133

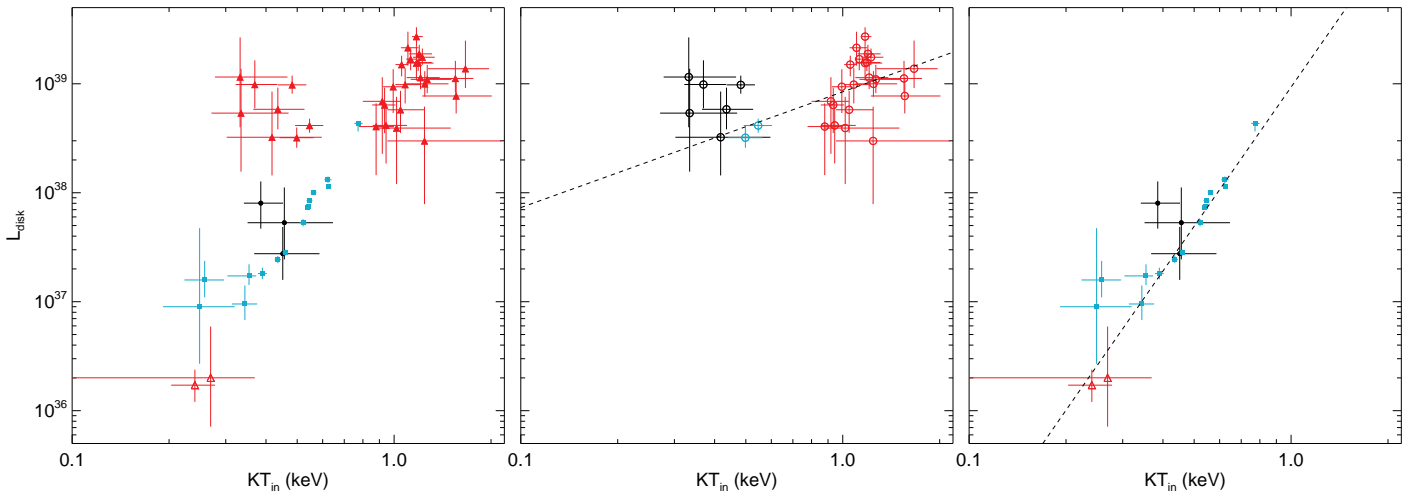


Figure 5. The disk luminosity $L_{\text{disk}} * D_{10}^{-2}$ vs. the disk inner temperature (kT_{in}). The dashed lines represent the best fitting relation. Left panel: the disk component of the whole outburst; different states are marked using the same colored symbols as Figure 3. Middle panel: the disk component in the high intermediate state (red filled triangles in left panel); black – first HIM state, red – SIM state, blue – second HIM state. Right panel: the disk component in the hard (black dots), soft (blue squares) and lower intermediate states (red opening triangles).

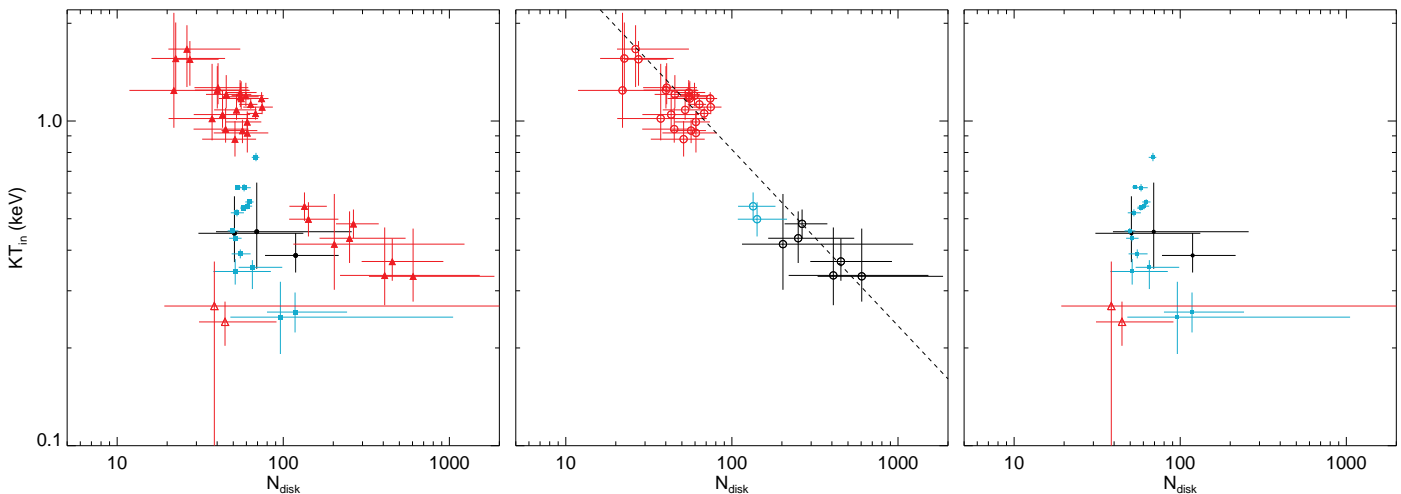


Figure 6. Disk inner temperature vs. the square root of the normalization of the diskbb model, $N_{\text{disk}} = R_{\text{in}}(\text{km}) * D_{10}^{-1} * \sqrt{\cos(i)}$. The dashed line represents the best fitting relation. Left panel: the disk component of the whole outburst; different states are marked using the same colored symbols as Figure 3. Middle panel: the disk component in the high intermediate state; different states are marked using the same colored symbols as Figure 5. Right panel: the disk component in the hard (black dots), soft (blue squares) and lower intermediate states (red opening triangles).

4 DISCUSSION

Swift monitoring observations and the detailed spectral analyses of the recently discovered BH candidate, MAXI J1535-571, are presented in this paper.

4.1 State evolution

The source was first detected in the hard state, then went through the high intermediate state, and reached the soft state afterward. Near the end of the outburst, the source went back to the low intermediate state and finally returned

to the hard state⁶. It shows a specific counter clockwise Q-shaped loop in the HIDs.

We track the evolution of the model parameters, such as N_{H} , Γ , T_{in} , N_{disk} and the component flux, during the outburst. N_{H} is larger than the Galactic value, suggesting that there are some intrinsic materials to obscure the source. Especially, N_{H} shows a peak around the peak of the outburst. We discuss the indication in Section 4.3. The power-law com-

⁶ Some most recent data reveal that the source has several state transitions at the end of the outburst (Parikh et al. 2018; Negoro et al. 2018). But the source flux is weak, we thus decide not to do detailed spectral analysis.

Table 2 – *continued*

ObsID	Model	N_{H} (10^{22} cm $^{-2}$)	Γ	kT_{in} (keV)	N_{disk}	χ^2/dof (C^2/dof) ^f
10264043	BB	$3.04^{+0.45}_{-0.40}$...	0.34 ± 0.03	51^{+33}_{-13}	100.9/63
10264044	BB	3^b	...	$0.26^{+0.04}_{-0.03}$	120^{+120}_{-40}	21.5/11
10264045	BB	$3.2^{+1.5}_{-1.1}$...	$0.25^{+0.07}_{-0.06}$	100^{+960}_{-50}	22.1/21
10264046	PLBB	$3.0^{+4.8}_{-0.9}$	1^{ce}	$0.27^{+0.10}_{-0.27}$	40^{+2030}_{-20}	11.1/9
10264047	PLBB	3^b	$1.0^{+8.7c}_{-0.0}$	0.24 ± 0.04	45^{+46}_{-13}	6.6/5
10264048 ^a	PL	$2.4^{+1.7}_{-1.3}$	$2.6^{+1.1}_{-1.0}$	58.7/63
10264049 ^a	PL	$2.8^{+2.8}_{-1.8}$	$1.1^{+0.9}_{-0.8}$	55.3/68
10264050 ^a	PL	3^b	$0.8^{+4.5d}_{-0.0}$	0.3/1
10264051 ^a	PL	3^b	$0.3^{+1.5}_{-1.9}$	4.3/10
10264052 ^a	PL	3^b	$0.4^{+2.2d}_{-0.0}$	3.2/4
10264053 ^a	PL	$4.2^{+2.0}_{-1.6}$	1.7 ± 0.6	120.6/159

^aUsing the C statistic (cstat in xspec) to fit the spectra.

^b N_{H} is fixed at 3×10^{22} cm $^{-2}$ as it is difficult to be constrained.

^cThe power-law component is weak and Γ favors a negative value when it is a free fit parameter. So, the lower limit of Γ is fixed to 1.

^dThe parameter lower limit and ^eupper limit are invalid due to a low statistic.

^fThe goodness of fit in C statistic is described in terms of C^2 .

ponent is weak in the soft state and is significant and harder in the hard state, while the disk component dominates the X-ray spectrum in the soft state and is weaker in the intermediate and hard states, consistent with the typical behaviors of Galactic black hole binaries.

4.2 Mass estimation

The spin of BH can be measured by fitting the disk continuum (Zhang et al. 1997), assuming a standard thin disk, or by fitting the general relativistic ray (e.g., García et al. 2014), and the normalization of the `diskbb` model can be used to infer the BH mass if giving the spin and inclination values. In the soft state, N_{disk} of MAXI J1535-571 is approximately constant, indicating that the inner disk extends to the ISCO. We thus use the measurements obtained in the soft state to estimate the BH mass. Assuming $a > 0.84$, $i = 57^\circ$ and $R_{\text{in}}(\text{km}) * D_{10}^{-1} * \sqrt{\cos(i)} = 50$, the BH mass is obtained to be larger than $14 M_{\odot}$ for a distance of 10 kpc, or greater than $7 M_{\odot}$ for a distance of 5 kpc. But we also note that the measurements of i and a are strongly dependent on the model, and the distance is unknown, thus the mass estimation here is only an estimate.

4.3 Eddington accretion

The peak flux of the source is up to ~ 5 Crab and its disk structure may be modified from the standard thin disk due to the high accretion rate. In order to investigate the physics of the accretion disk, we have examined the relationship between disk luminosity and temperature, $L_{\text{disk}} \propto T_{\text{in}}^{\alpha}$, and the radial emission profile of the disk temperature, $T(R) \propto R^{-p}$. We found $\alpha \sim 1$ and $p \sim 0.5$ in the high intermediate state (middle panels of Figures 5 and 6), in contrast with the expectations of a simple thin disk, but consistent with a slim disk (Abramowicz et al. 1988). In the remaining states, an α of 4.24 ± 0.11 well agrees with the value of a standard thin disk. Therefore, we replace the `diskbb` model in the high

intermediate state with a disk model with a variable exponent to the disk temperature profile, i.e., p -free disk model (`diskpbb`)⁷ in XSPEC. The p expected for a standard thin disk is 0.75, while for a slim disk, is 0.5. If a power law is added to the p -free disk model, we are not able to constrain p in the spectral fits, and all possible p values, from 0.5 to 1.0, are allowed. If the p -free model is used alone, p appears to be ~ 0.5 , consistent with the expectations of a slim disk. If we fix p of `diskpbb` at 0.5 and fit the spectra again⁸, T_{in} and N_{disk} would be subject to a power-law function with an index of 0.63 ± 0.03 (Figure 7). If only fitting the data in the SIM state, the index would be 0.56 ± 0.09 . Moreover, we note that N_{disk} in the SIM state is smaller than that of the soft state, which is seemingly unreasonable because the inner disk already extends to the ISCO in the soft state. However, for a high accretion rate, the advection-dominated flow does not abruptly decrease inside the ISCO. An amount of matter inside the ISCO can produce a substantial radiation, thus the derived inner disk radius is smaller than that of the ISCO (Watarai et al. 2000).

The slim disk is dominated by the advection within the disk, and becomes radiatively inefficient due to the advection process, resulting in the flattening of the L_{disk} and T_{in} relationship. p , in the radial emission profile, is expected as 0.5 for a slim disk (Watarai et al. 2000). A slim disk exists when the luminosity is close to the Eddington or moderately super-Eddington. The disk luminosity of MAXI J1535-571, in the high intermediate state, is larger than 10^{38} erg s $^{-1}$ and could reach up to several of 10^{39} erg s $^{-1}$, approaching to or exceeding the Eddington limit of a stellar mass BH. As a result of this high accretion rate, the disk of MAXI J1535-571 cannot maintain its thin geometry, and becomes slim. The slim accretion disk has also been suggested for a few

⁷ <https://heasarc.gsfc.nasa.gov/xanadu/xspec/manual/node164.html>

⁸ It is difficult to constrain the power-law index for some observations, and a negative value is obtained if fitting the component freely. We thus set the lower limit of the power-law index to be 1.

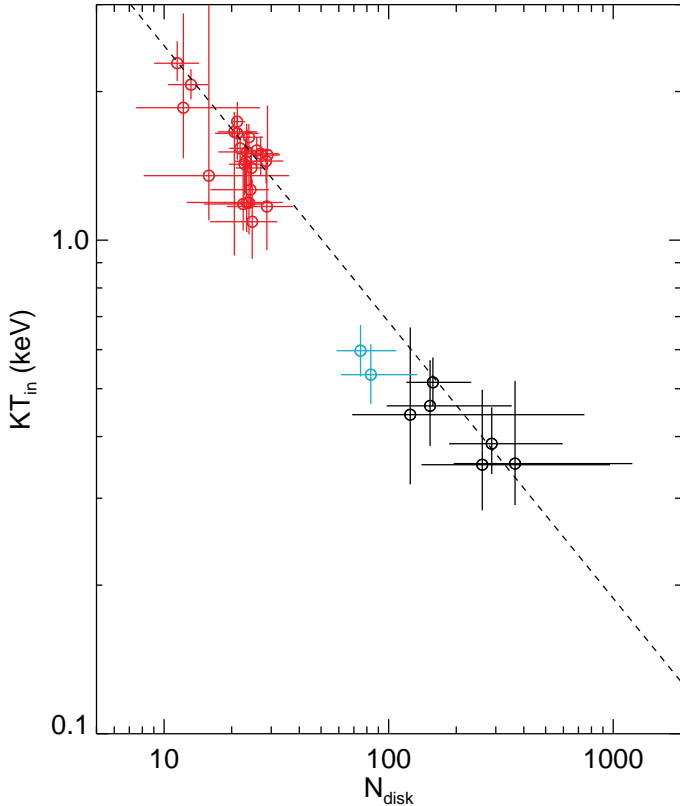


Figure 7. Disk inner temperature vs. the square root of the normalization of the `diskpbb` model. Different intermediate states are marked using the same colored symbols as Figure 5.

Galactic BH binaries in high state, such as XTE J1550-564 (Kubota & Makishima 2004), 4U 1630-47 (Tomsick et al. 2005) and V404 Cyg (Motta et al. 2017), and also for some Ultraluminous X-ray sources (Kaaret et al. 2017).

In usually, as the mass accretion rate increases, the radiation pressure begins to dominate and an outflow is blown from the disk, which can obscure the source and increase N_{H} . Actually, N_{H} in MAXI J1535-571 is larger than the Galactic column density, and shows an evolution in the outburst with a peak around the flux maxima. We thus test the correlation (Figure 8) between N_{H} and the Eddington ratio assuming a BH mass of $10 M_{\odot}$, which is an average estimation above. N_{H} keep about $3 \times 10^{22} \text{ cm}^{-2}$ when unabsorbed R_{Edd} (upper panel of Figure 8) is low (< 0.1) and start to increase as the increasing of R_{Edd} , consistent with the scenario that outflows are driven by high accretion rate. Especially in high intermediate state, N_{H} is significantly larger. However, we also note that there is a degeneracy between N_{H} and unabsorbed R_{Edd} , as a higher N_{H} will recover a larger unabsorbed R_{Edd} . Therefore, we test the correlation between N_{H} and observed R_{Edd} , and found that high observed R_{Edd} also correspond to large N_{H} . Moreover, except for observations that the source are in the hard source, N_{H} also seems to be correlated with the unabsorbed R_{Edd} of disk component, and starts to enhance around several percent of R_{Edd} .

Blueshifted X-ray absorption features are discovered in some super-Eddington sources (Pinto et al. 2016; Walton et al. 2016), and explained as originating in a wind

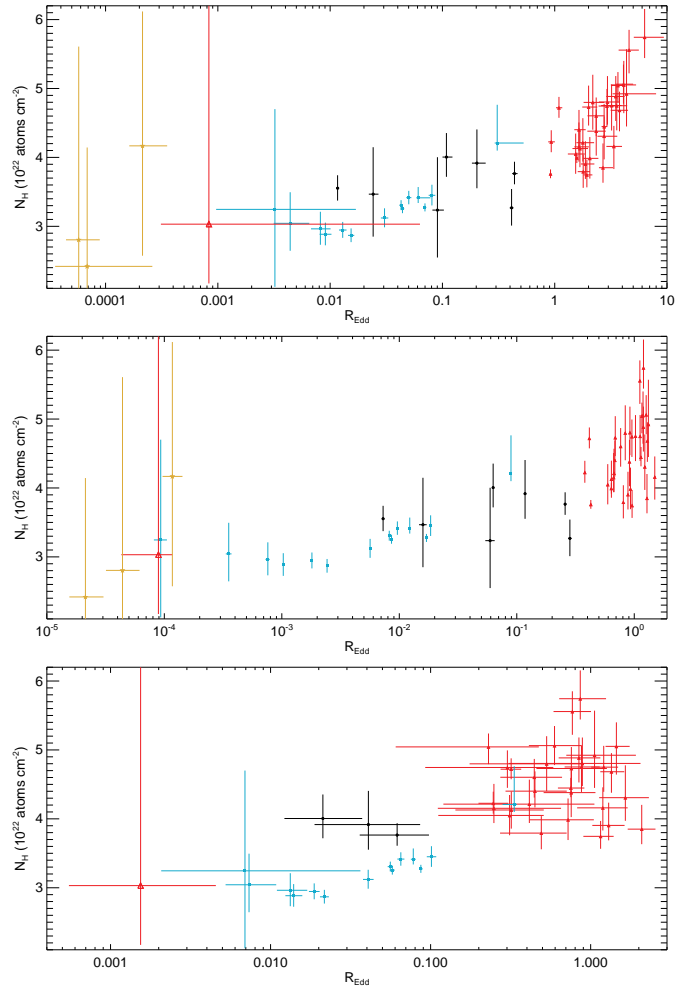


Figure 8. N_{H} vs. Eddington ratio. upper: unabsorbed source Eddington ratio in the 0.5–10.0 keV band; middle: observed source Eddington ratio in the 0.5–10.0 keV band; lower: unabsorbed disk Eddington ratio. Different states are marked using the same colored symbols as Figure 3.

flowing toward us. For MAXI J1535-571, some low-energy line-like residuals, such as an absorption feature at ~ 2.0 keV and an emission feature at ~ 2.3 keV, appear in the spectra (Figure 9). But the detections of the line features are marginal⁹, and we note that the residuals near the Silicon and Gold edges (~ 2 keV) were previously observed in some XRT spectra¹⁰. Although the improved calibration files have reduced the residuals, in a few cases, the feature is still apparent. Therefore, we do not go further in this paper based on the current data quality. High spectral resolution data are needed to further resolve the feature in MAXI J1535-571.

ACKNOWLEDGMENTS

We thank the anonymous referee for useful comments that have improved the paper. LT acknowledges funding sup-

⁹ The line feature is so weak that it will not affect the continuum fitting results.

¹⁰ http://www.swift.ac.uk/analysis/xrt/digest_cal.php#res

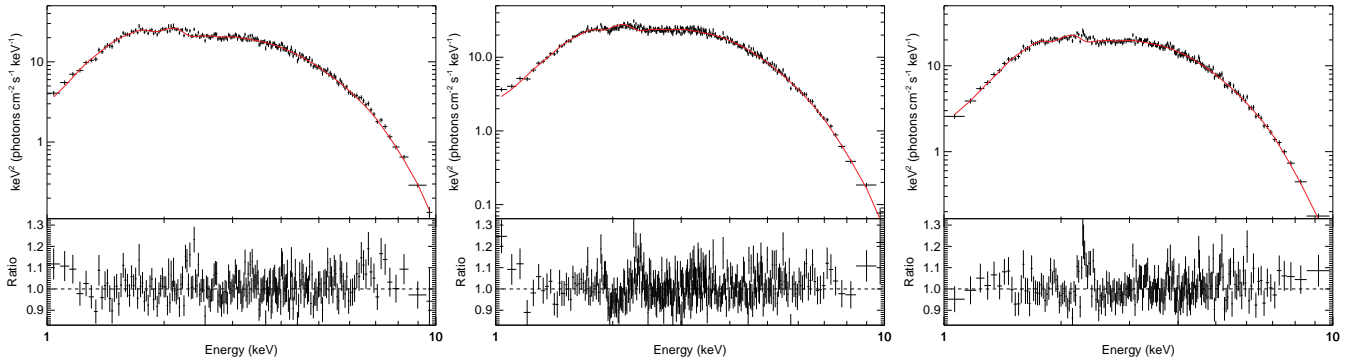


Figure 9. Examples of line-like spectral features. The data were grouped to have a signal-to-noise ratio of at least 15 per bin. Left: ObsID 10264007; middle: ObsID 102640012; right: ObsID 88245003.

port from the National Natural Science Foundation of China (NSFC) under grant numbers U1838115, the CAS Pioneer Hundred Talent Program Y8291130K2 and the Scientific and technological innovation project of IHEP Y7515570U1. CG acknowledges support from CAS President’s International Fellowship Initiative (PIFI). JQ thank support from the Chinese NSFC 11673023. We thank support from National Key R&D Program of China (grant No. 2016YFA0400800), the Chinese NSFC U1838201, 11733009 and 11473027, XTP project XDA 04060604, the Strategic Priority Research Programme ‘The Emergence of Cosmological Structures’ of the Chinese Academy of Sciences, Grant No.XDB09000000, and the Chinese NSFC U1838202.

REFERENCES

- Abramowicz, M. A., Czerny, B., Lasota, J. P., & Szuszkiewicz, E. 1988, *ApJ*, 332, 646
- Arnaud, K. A. 1996, *Astronomical Data Analysis Software and Systems V*, 101, 17
- Barthelmy, S. D. 2004, *Proc. SPIE*, 5165, 175
- Belloni, T., Homan, J., Casella, P., et al. 2005, *A&A*, 440, 207
- Belloni, T. M., & Motta, S. E. 2016, *Astrophysics of Black Holes: From Fundamental Aspects to Latest Developments*, 440, 61
- Britt, C. T., Bahramian, A., & Strader, J. 2017, *The Astronomer’s Telegram*, 10816,
- Burrows, D. N., Hill, J. E., Nousek, J. A., et al. 2005, *SSRv*, 120, 165
- Dauser, T., García, J., Parker, M. L., Fabian, A. C., & Wilms, J. 2014, *MNRAS*, 444, L100
- Dincer, T. 2017, *The Astronomer’s Telegram*, 10716,
- Done, C., Gierliński, M., & Kubota, A. 2007, *A&AR*, 15, 1
- Fender, R. P., Belloni, T. M., & Gallo, E. 2004, *MNRAS*, 355, 1105
- García, J., & Kallman, T. R. 2010, *ApJ*, 718, 695
- García, J., Dauser, T., Lohfink, A., et al. 2014, *ApJ*, 782, 76
- Gendreau, K. C., Arzoumanian, Z., & Okajima, T. 2012, *Proc. SPIE*, 8443, 844313
- Gendreau, K., Arzoumanian, Z., Markwardt, C., et al. 2017, *The Astronomer’s Telegram*, 10768,
- Harrison, F. A., Craig, W. W., Christensen, F. E., et al. 2013, *ApJ*, 770, 103
- Huang, Y., et al. 2018, submitted
- Kaaret, P., Feng, H., & Roberts, T. P. 2017, *ARA&A*, 55, 303
- Kalberla, P. M. W., Burton, W. B., Hartmann, D., et al. 2005, *A&A*, 440, 775
- Kennea, J. A., Evans, P. A., Beardmore, A. P., et al. 2017, *The Astronomer’s Telegram*, 10700,
- Kennea, J. A. 2017, *The Astronomer’s Telegram*, 10731,
- Kubota, A., & Makishima, K. 2004, *ApJ*, 601, 428
- Lasota, J.-P. 2001, *NewAR*, 45, 449
- Markwardt, C. B., Burrows, D. N., Cummings, J. R., et al. 2017, *GCN CIRCULAR*, 21788
- Matsuoka, M., Kawasaki, K., Ueno, S., et al. 2009, *PASJ*, 61, 999
- Mereminskiy, I. A., & Grebenev, S. A. 2017, *The Astronomer’s Telegram*, 10734,
- Mereminskiy, I. A., Grebenev, S. A., Prosvetov, A. V., & Semena, A. N. 2018, arXiv:1806.06025
- Miller, J. M., Gendreau, K., Ludlam, R. M., et al. 2018, arXiv:1806.04115
- Motta, S. E., Kajava, J. J. E., Sánchez-Fernández, C., et al. 2017, *MNRAS*, 471, 1797
- Nakahira, S., Negoro, H., Mihara, T., et al. 2017, *The Astronomer’s Telegram*, 10729,
- Nakahira, S., Shidatsu, M., Makishima, K., et al. 2018, arXiv:1804.00800
- Negoro, H., Ishikawa, M., Ueno, S., et al. 2017a, *The Astronomer’s Telegram*, 10699,
- Negoro, H., Kawase, T., Sugizaki, M., et al. 2017b, *The Astronomer’s Telegram*, 10708,
- Negoro, H., Sugawara, Y., Nakajima, M., et al. 2018, *The Astronomer’s Telegram*, 11682,
- Palmer, D. M., Krimm, H. A., & Swift/BAT Team 2017, *The Astronomer’s Telegram*, 10733,
- Parikh, A. S., Russell, T. D., Wijnands, R., et al. 2018, *The Astronomer’s Telegram*, 11652,
- Pinto, C., Middleton, M. J., & Fabian, A. C. 2016, *Nature*, 533, 64
- Remillard, R. A., & McClintock, J. E. 2006, *ARA&A*, 44, 49
- Revnivtsev, M., Gilfanov, M., Churazov, E., & Sunyaev, R. 2002, *A&A*, 391, 1013
- Russell, T. D., Miller-Jones, J. C. A., Sivakoff, G. R., Tetarenko, A. J., & Japote Xrb Collaboration 2017, *The Astronomer’s Telegram*, 10711,

- Russell, T. D., Altamirano, S. R. D., Miller-Jones, J. C. A., et al. 2018, The Astronomer's Telegram, 11611,
- Scaringi, S., & ASTR211 Students 2017, The Astronomer's Telegram, 10702,
- Shang, J. R. et al. 2018, arXiv:1806.07147
- Shakura, N. I., and Sunyaev, R. A., *A&A*, 24, 337–355(1973).
- Shidatsu, M., Nakahira, S., Negoro, H., et al. 2017, The Astronomer's Telegram, 10761,
- Tetarenko, A. J., Russell, T. D., Miller-Jones, J. C. A., Sivakoff, G. R., & Jacpot Xrb Collaboration 2017, The Astronomer's Telegram, 10745,
- Tomsick, J. A., Corbel, S., Goldwurm, A., & Kaaret, P. 2005, *ApJ*, 630, 413
- Verner, D. A., Ferland, G. J., Korista, K. T., & Yakovlev, D. G. 1996, *ApJ*, 465, 487
- Walton, D. J., Middleton, M. J., Pinto, C., et al. 2016, *ApJL*, 826, L26
- Watarai, K.-y., Fukue, J., Takeuchi, M., & Mineshige, S. 2000, *PASJ*, 52, 133
- Wilms, J., Allen, A., & McCray, R. 2000, *ApJ*, 542, 914
- Xu, Y., Harrison, F. A., García, J. A., et al. 2018, *ApJL*, 852, L34
- Zhang, S. N., Cui, W., & Chen, W. 1997, *ApJL*, 482, L155